



## Research Paper

## Laser beam welding of dual-phase DP1000 steel

P.H.O.M. Alves<sup>a</sup>, M.S.F. Lima<sup>b</sup>, D. Raabe<sup>c</sup>, H.R.Z. Sandim<sup>a,\*</sup><sup>a</sup> Lorena School of Engineering, University of Sao Paulo, Lorena, SP, 12602-810, Brazil<sup>b</sup> Institute of Advanced Studies, IEAv, Sao Jose dos Campos, SP, 12227-000, Brazil<sup>c</sup> Max-Planck-Institut für Eisenforschung, D-40237, Düsseldorf, Germany

## ARTICLE INFO

## Keywords:

Laser beam welding  
Dual-phase steel  
DP1000 steel  
Phase transformation  
Microstructural characterization  
EBSD

## ABSTRACT

Autogeneous laser beam welding is an efficient process to join ferritic-martensitic dual-phase steels without large dimensional distortions. Localized softening may occur in the heat affected zone, particularly in DP1000 steel with a high martensite volume fraction. DP1000 steel was welded in bead-on-plate configuration varying the welding power between 0.4 and 2.0 kW and the welding speed between 20 and 150 mm/s. Light optical microscopy, scanning electron microscopy, and X-ray diffraction were used to perform the microstructural characterization of the welded joints. High-quality laser beam welds of thin sheets of DP1000 steel can be produced using appropriate welding parameters. The optimal welding condition was a nominal laser power of 2.0 kW and a welding speed of 150 mm/s. This condition minimizes the amount of softening of prior martensite and yields a narrow heat affected zone and a small volume fraction of retained austenite in the weld.

## 1. Introduction

The literature on laser beam welding (LBW) of DP steels focuses mostly on mechanical behavior and microstructural changes caused for this process. Parkes et al. (2014) reported the mechanical properties of the fiber-laser welded joints of DP980 steel (similar to DP1000) at cryogenic, room, and elevated temperatures. They observed lower strain values to failure caused by the presence of the so-called soft zone (SZ) localized at the heat affected zone (HAZ). Similar findings have been previously reported by Xu et al. (2012) in their study on microstructure, mechanical properties, and fatigue behavior of DP980 steel. In these works, softening is explained by either tempering of prior martensite or its decomposition at the subcritical HAZ. Bandyopadhyay et al. (2015) investigated the limiting drawing ratio (LDR) and deep drawing behavior of dissimilar tailor welded blanks (TWBs) in DP steels using finite element method (FEM). The simulation was performed using the parent metal anisotropy and weld zone properties to predict premature failure. The results showed a non-uniform deformation behavior with localized necking/failure initiation in the softer material (DP600). The optimization of the welding parameters to minimize localized softening in the HAZ of DP980 steel was also investigated by Bandyopadhyay et al. (2016a,b). They applied the response surface methodology (RSM) to define optimized laser welding parameters (power, speed, focal position and roughness) to manufacture DP980 TWBs. The work reported a reduction of 67% in the SZ width and 55% of softening for a full penetration weld. However, strain localization

and subsequent failure still occurred in the SZ. Xia et al. (2008) used the normalized Rosenthal's equation and Vickers hardness testing to investigate to effect of heat input and martensite volume fraction on the HAZ softening of DP steels. The study shows a proportional relationship between the extent of HAZ softening and martensite volume fraction caused by tempering of martensite. Biro et al. (2010) examined how chemistry and microstructure of DP600 and DP780 steel grades affect martensite tempering kinetics during laser welding. They observed that the product of martensite decomposition at the HAZ, for all investigated welds, was cementite, and the softening kinetics fitted to the Avrami equation. Baltazar-Hernandez et al. (2011) reported the same cementite effect on softening phenomenon. Other common observation was the increase of the resistance to softening provided by carbide-forming alloying elements such as chromium and molybdenum. The precipitation of carbides during tempering of martensite was also reported by Wang et al. (2016) using a Gleeble thermomechanical simulator to reproduce weld thermal cycles in all subzones of the HAZ of laser-welded DP1000 steel. They also reported a decrease of the dislocation density in prior ferrite and a second softening stage at the intercritical HAZ. This secondary softening can be attributed to the decrease of martensite fraction and the appearance of bainite and martensite-austenite (M-A) constituents. Some residual austenite also remains in the microstructure.

Therefore, there is still need for a more detailed investigation of the effects of the main welding parameters (welding power and speed) on the microstructural changes that directly affect the mechanical

\* Corresponding author.

E-mail address: [hsandim@demar.eel.usp.br](mailto:hsandim@demar.eel.usp.br) (H.R.Z. Sandim).

**Table 1**

Chemical composition (wt%) and mechanical properties of DP1000 steel where YS is the yield strength, TS is the tensile strength, E is the elongation,  $\bar{R}$  is the normal anisotropy, and  $\Delta R$  the planar anisotropy.

C	Si	Mn	P	S	Cr	Ni	Mo	Al	Cu	Co
0.151	0.534	1.507	0.0112	0.0030	0.062	0.066	0.031	0.038	0.0046	0.0172
Ti	Nb	V	B	YS (MPa)	TS (MPa)	YS/TS	E (%)	$\bar{R}$	$\Delta R$	
0.0019	0.0113	0.0049	0.00065	711	1018	0.70	12	0.68	0.08	

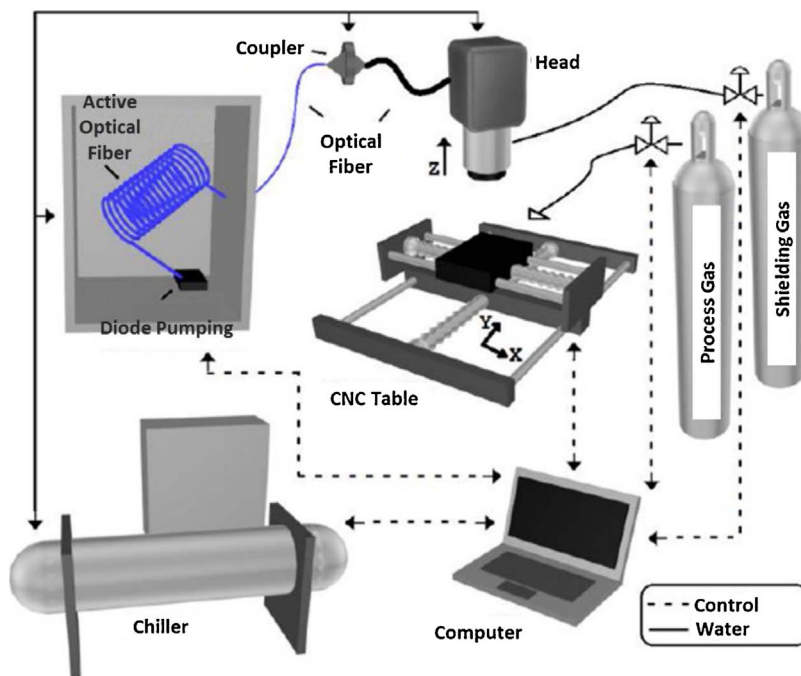


Fig. 1. Schematic diagram of the fiber laser beam welding station used in the present investigation.

behavior of ultra-high-strength dual-phase steels, such as DP1000.

A detailed characterization was performed to follow the microstructural changes with aid of light optical microscopy (LOM) and scanning electron microscopy (SEM). High-resolution electron backscatter diffraction (EBSD) was used for the quantification of retained austenite and its distribution in the weld. Representative specimens were also subjected to conventional tensile testing to evaluate the mechanical behavior of the welds.

## 2. Experimental

### 2.1. Material

The material investigated was a commercial uncoated cold-rolled DP1000 steel supplied by Swedish Steel AB (SSAB) with a thickness of 1.8 mm. The full chemical composition determined by optical emission spectroscopy (OES) and the mechanical properties of this steel are shown in Table 1. Thermodynamic calculations were performed with the Thermo-Calc<sup>®</sup> software using the TCFE-7 database for prediction and quantification of the phases and their corresponding transformation temperatures. The carbon equivalent content (in wt%), CE, was determined using the equation proposal by Yurioka et al. (1983) that predicts the weldability of steels. This versatile expression has an accommodation factor,  $A(C)$ , which is a function of the carbon content of the steel.

$$CE = C + A(C) \cdot \left\{ \frac{Si}{24} + \frac{Mn}{6} + \frac{Cu}{15} + \frac{Ni}{20} + \frac{Cr + Mo + Nb + V}{5} + 5B \right\} \quad (1)$$

where:

$$A(C) = 0.75 + 0.25 \cdot \tanh\{20(C - 0.12)\} \quad (2)$$

### 2.2. Laser beam welding

Autogenous bead-on-plate welding was performed on DP1000 steel sheets in the keyhole mode simulating a butt joint without a gap. Welds were made using an IPG Photonics Yb-fiber laser system model YLR-2000 with a wavelength of 1080 nm. The plate was placed on a CNC-driven table with servomotors controlled by a computer allowing for a maximum resolution of 5  $\mu$ m in the x-y axis and 1  $\mu$ m in the z-axis (vertical) that controls the focal length. Nitrogen and argon gases were used for optical and weld pool protection, respectively. Argon gas flow rate was 6.6 L/min. Fig. 1 shows a schematic drawing of the laser beam welding station used in the present investigation.

### 2.3. Microstructural and mechanical characterization

Quantitative metallography based on image analysis was used to determine the volume fractions of ferrite and martensite as well as

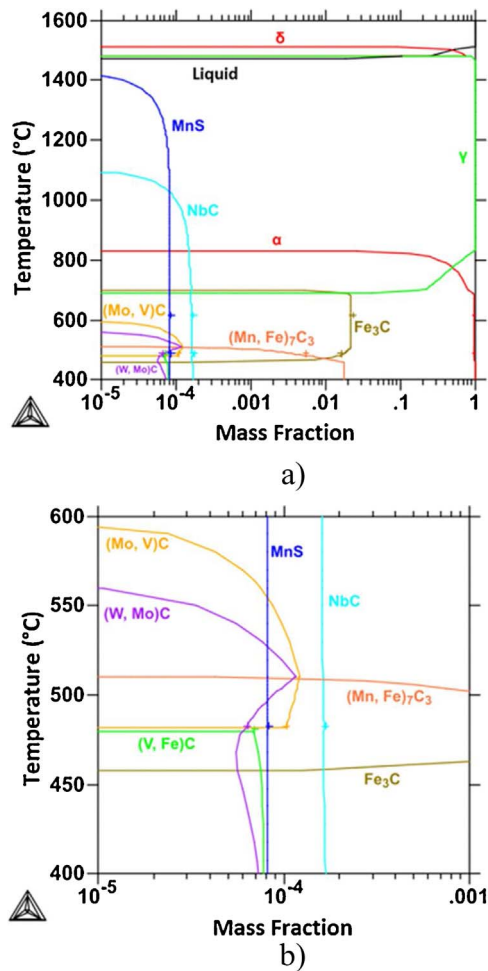


Fig. 2. Thermodynamic equilibrium of the DP1000 steel: a) Volume fraction of the phases from 400 °C up to the liquidus temperature; and b) Detailed view of the expected phases in the temperature range 400–600 °C.

ferrite mean grain size in the base metal (BM). Similar strategy was also adopted by Saeidi et al. (2014) to evaluate the volume fraction of microconstituents in DP steels. Zhang et al. (2016) used a similar approach

to determine the distribution of martensite in DP980 steel. Vickers hardness profiles were obtained from base metal toward the fusion zone (FZ) with a load of 100 gf for 10 s.

Phase identification and microtexture analysis were performed in a high-resolution EBSD system coupled to a field emission gun scanning electron microscope (FEG-SEM) JEOL model JSM-6500 operating at 25–30 kV and using a step size of 50 nm. The amounts of retained austenite in the base metal and in representative welds were determined by X-ray diffraction (XRD) in a Seifert-type ID3003 diffractometer with Co-K $\alpha_1$  radiation ( $\lambda = 0.178897$  nm) using a capillary with a beam diameter of 0.70 mm. The acquisitions were made every  $\Delta 2\theta = 0.05^\circ$  with a time of 60 s (40 kV, 30 mA). Quantification of retained austenite was made by Rietveld refinement using MAUD software version 2.33.

Tensile tests were conducted on polished specimens in an EMIC<sup>®</sup> model DL10000 electromechanical testing machine with an EMIC<sup>®</sup> Trd 2 model 50-mm extensometer. Five individual tests were conducted for each weld condition to enhance statistics. All tensile tests were performed according to ASTM E8/E8M-11 with a speed of 1 mm/min for 50 mm gage length in the transverse direction (TD).

### 3. Results and discussion

#### 3.1. Thermodynamic calculations

Fig. 2a shows the expected volume fraction of the phases provided by thermodynamic calculation of DP1000 steel. The simulation shows the onset of solidification at 1510 °C (*liquidus* temperature) with the appearance of  $\delta$ -ferrite phase. The steel solidifies completely at 1460 °C (*solidus* temperature) as austenite. Between 1460 °C and 832 °C ( $A_{c3}$  temperature) the appearance of a MnS compound is noticed. From 832 °C to 685 °C ( $A_{c1}$  temperature) the ferrite and austenite phases coexist with cementite (Fe<sub>3</sub>C). Below 685 °C the material consists of  $\alpha$ -ferrite and several compounds dispersed in the matrix (Mn, Fe)<sub>7</sub>C<sub>3</sub>, NbC, (Mo, V)C, (W, Mo)C and WC (Fig. 2b). Depending on their kinetics of phase formation, these minor compounds appear in the microstructure as fine particles leading to grain refinement and ferrite hardening. The calculated equivalent carbon content for the studied material is 0.42%, slightly above the limit of 0.40% cited in the literature (Easterling, 1992), but high enough to display a slight tendency to form martensite upon cooling in welds without preheating.

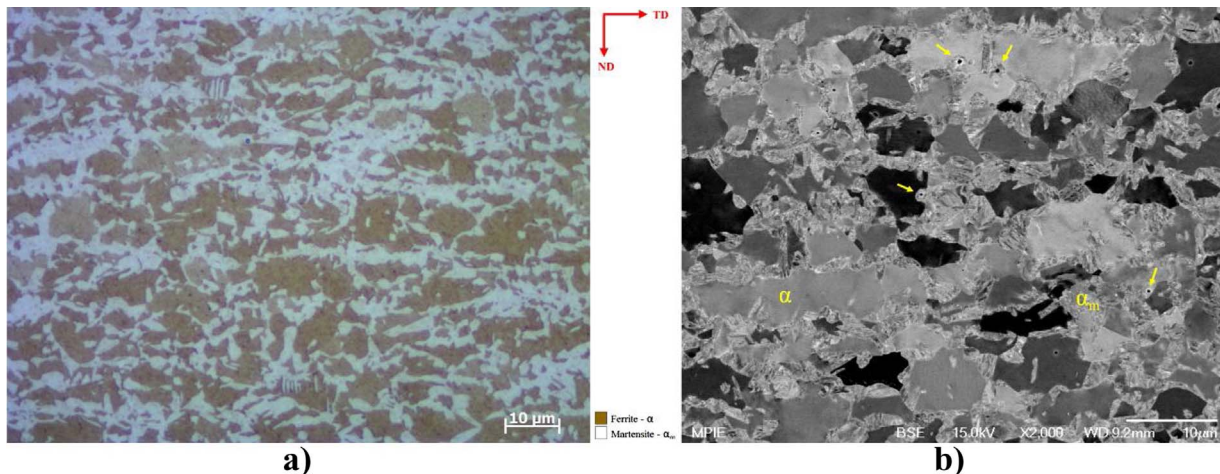


Fig. 3. Micrographs of the cross-section (TD-ND plane) of the DP1000 steel showing the microconstituents ferrite and martensite: a) Light optical microscopy image after modified LePera etching; and b) Scanning electron microscopy with backscattered electrons image. TD e ND refer to the transverse and to the normal directions, respectively.



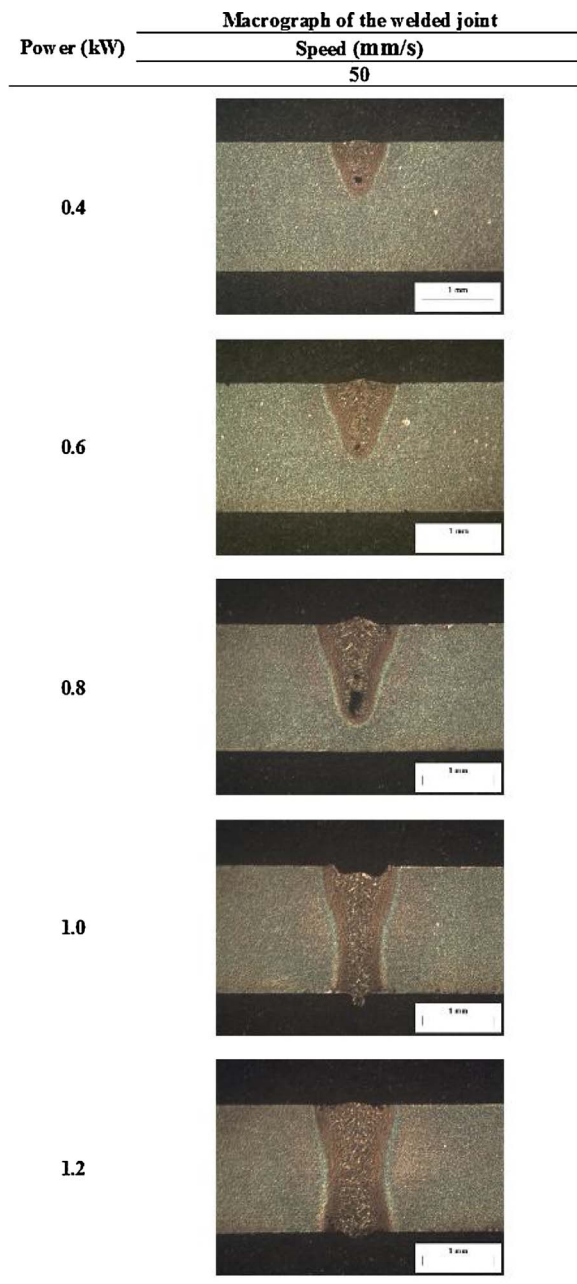


Fig. 4. Weld profiles as a function of welding power for a constant travel speed of 50 mm/s. TD and ND refer to the transverse and to the normal directions, respectively.

### 3.2. Microstructure of base metal

DP1000 steel has a volume fraction of  $43 \pm 4\%$  of martensite and ferrite mean grain size of  $3.0 \pm 0.4 \mu\text{m}$ . Vickers hardness varied from  $330 \pm 17 \text{ HV}$  when probed in the cross-section to  $355 \pm 17 \text{ HV}$  in the longitudinal section. Fig. 3a shows the morphology and distribution of ferrite grains in the cross-section of the welds (TD-ND plane). Ferrite grains have a degenerate morphology caused by nucleation and growth of austenite and further martensite formation at grain boundaries upon cooling. Other nucleation sites besides grain boundaries are noticeable in Fig. 3b. The particle-matrix interfaces act as preferential nucleation

sites as noticed in the martensite islands formed around coarse inclusions indicated by yellow arrows in the SEM micrograph. Bleck and Phiu-On (2005) defines as “dual-phase” the family of steels composed of a ferritic matrix with the presence of dispersed martensite islands. However, in DP1000 steel, the high volume fraction of martensite makes this definition a bit controversial because almost all ferrite is encompassed by martensite forming a contiguous microstructure, which is better described as a network-like microstructure.

### 3.3. Bead-on-plate welding

In the first batch of tests, the steel sheet was welded with a constant travel speed of 50 mm/s varying the laser power between 0.4 and 1.2 kW, as shown in Fig. 4. For powers of 1.0 kW and 1.2 kW full penetration was observed, but the weld produced with 1.0 kW was narrower than the one with 1.2 kW. When welding is performed with powers of 0.4, 0.6 and 0.8 kW only partial penetration is noticed. Besides partial penetration, internal porosity was also noticed in their corresponding weld roots. According to Zhou and Tsai (2007), the presence of pores in the FZ is associated with the weld pool dynamics, keyhole collapse, and solidification processes in LBW, which restricts the flow of molten metal towards the center of the keyhole before solidification. Meng et al. (2014) also confirm the effect of the keyhole collapse process on the formation of porosity in lap joints of laser welded high-strength low-alloy (HSLA) steels. The authors also suggest that gas bubbles are generated during welding at the tip of the keyhole. These bubbles are entrained by the strong liquid metal flow being trapped by the rapidly progressing solidification front resulting in closed porosity, as observed in the current study.

A second batch of tests was carried out by varying the welding speed between 20 and 150 mm/s for constant laser power values of 0.8 and 1.0 kW; i.e., within a range where welds have either partial or full penetration (Fig. 5). For 0.8 kW only the speed of 20 mm/s leads to full penetration. The welds produced with a laser power of 1.0 kW showed full penetration for speeds between 20 and 70 mm/s. However, significant differences in the width of the HAZs can be noticed; i.e., the higher the travel speed, the narrower is the HAZ. This inverse relationship between welding speed and width of the HAZ was also observed by Benyounis et al. (2005) in their study on heat input effects in the weld profile. In the third batch of tests, LBW was carried out with 2.0 kW and 150 mm/s producing the narrowest weld bead. For sake of identification and traceability, welds were named according to their nominal values of power and speed, as follows: PXX/SYYY, where P indicates the power XX (kW), and S refers to the welding speed YYY (mm/s).

Fig. 6 shows the variation of thickness-normalized heat input proposed by Xia et al. (2008) for LBW using the analytical Rosenthal's solution. The values were obtained using the experimental width of the welds with full penetration. P2.0/S150 weld presented the lowest heat input and the lowest variation of width across the thickness with a ratio width/thickness of 0.30. The calculated values of heat input increase monotonically from P2.0/S150 to P1.0/S20 weld as well as the variation in weld bead width.

### 3.4. Hardness profiles

Following macrographic examination, Vickers microhardness measurements were performed in the cross-section of P1.0/S20 (broadest HAZ), P1.2/S50 (intermediary HAZ) and P2.0/S150 (narrowest HAZ) welds aiming at evaluating the presence of soft zones. The blue line indicates the mean hardness taken at the cross-section of the BM. The dashed red line marks the lowest hardness values found in BM taking

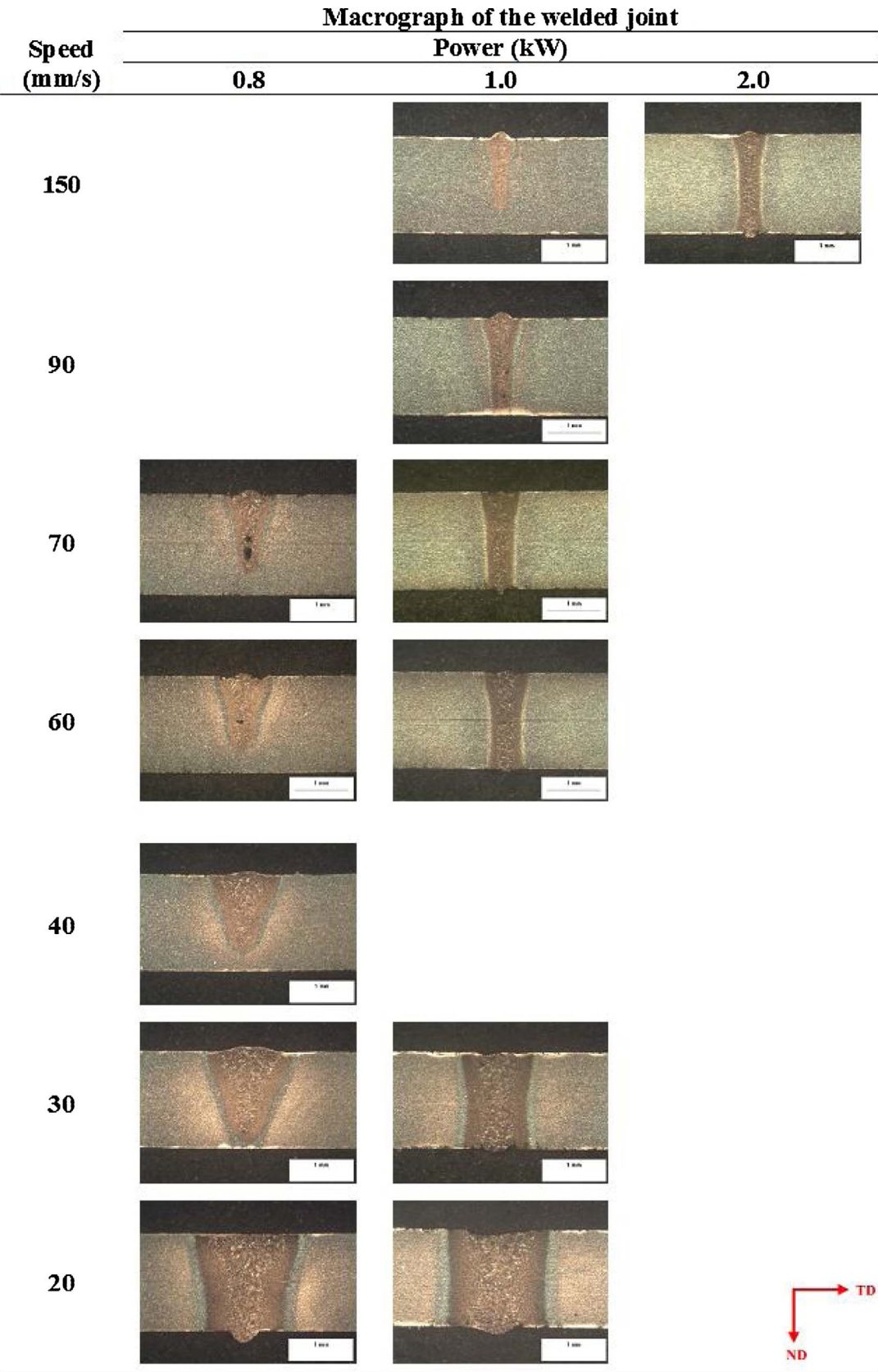


Fig. 5. Changes in the weld profiles as a function of welding power and speed. TD and ND refer to the transverse and to the normal directions, respectively.

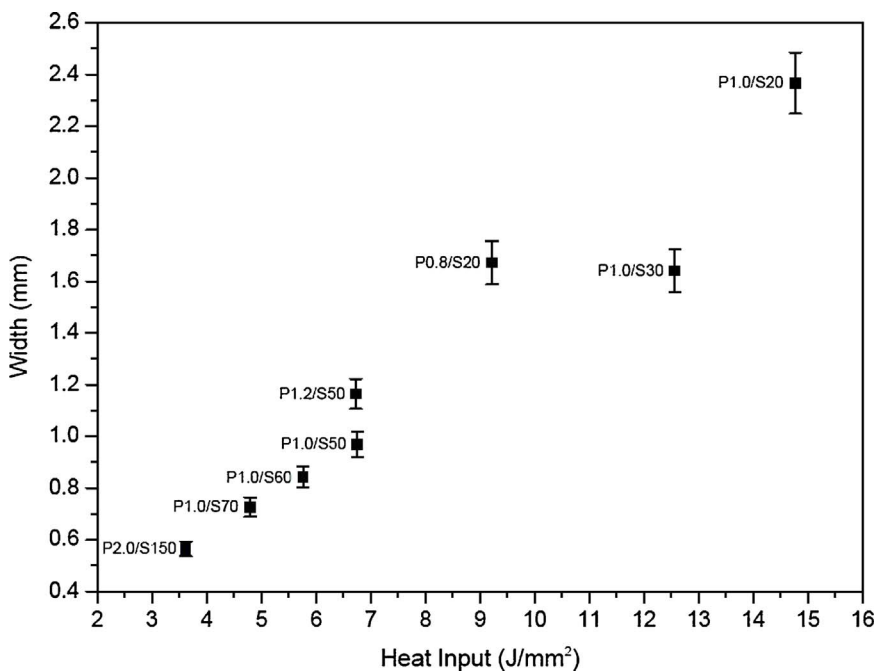


Fig. 6. Calculated heat input as a function of the weld bead width.

into account their standard deviation. P1.0/S20 weld (Fig. 6a) displayed a maximum value of 486 HV in the FZ and a minimum of 270 HV in the HAZ, precisely between the intercritical and subcritical HAZs. These values represent amounts of hardening and softening of about 47% and 18%, respectively, compared to the BM.

P1.2/S50 weld (Fig. 7b) showed maximum and minimum hardness values of 267 HV and 476 HV, respectively. These values indicate 44% of hardening and 19% of softening, similar to those observed in P1.0/S20 weld. On the other hand, P2.0/S150 weld (Fig. 7c) has a maximum hardness of 500 HV in the FZ and 320 HV in the HAZ, corresponding to amounts of hardening and softening of about 52% and 3%, respectively, compared to the BM. Therefore, P2.0/S150 weld is the most resistant joint and displays the lower amount of softening in the HAZ. Based on these results, it was also possible to estimate the length of the regions that underwent more softening. While P2.0/S150 weld displays the lowest amount of softening in the HAZ, P1.0/S20 and P1.2/S50 welds showed softened regions in the vicinity of the welds of about 1.50 and 0.75 mm wide, respectively. Bandyopadhyay et al. (2016a,b) reported that DP980 steel also exhibits a marked softening in the HAZ due to tempering of prior martensite. Zhao et al. (2013) also have reported that the extent of softening depends on the volume fraction of martensite in the BM. In case of DP steels the extent of HAZ softening increases with steel grade because of the larger higher martensite volume fraction. Their work also showed that tempering duration time was proportional to the inverse square of the welding speed. Thus, the decrease of welding speed causes longer tempering times and higher degrees of HAZ softening.

### 3.5. Tensile tests

Fig. 8 shows the engineering stress-strain curves of P1.0/S20 and P2.0/S150 welds and BM and their respective failure localization. These two welds were chosen because they had the largest and smallest bead width values. Compared to the BM, these welds showed a remarkable reduction in elongation. BM and P2.0/S150 weld showed values of tensile strength of  $1017 \pm 6$  MPa and  $1033 \pm 6$  MPa, respectively,

corresponding to a joint efficiency of 102%. Fracture of P2.0/S150 weld occurred in the BM, not in the HAZ. The joint efficiency is a parameter defined as the ratio of the tensile strength of the weld to the tensile strength of the corresponding BM (ASM Committee, 1993). P1.0/S20 weld had a tensile strength of  $991 \pm 7$  MPa, slightly lower than the minimum admissible value specified for DP1000 steel (1000 MPa), giving a joint efficiency of 97%, as similarly reported in the literature by Parkes et al. (2013) in DP980 steel. P1.0/S20 weld fractured at the HAZ confirming a localized embrittlement (Fig. 7a). If the acceptance criterion established in AWS D1.1 standard (AWS Committee, 2015) is adopted, the fracture in the HAZ can be accepted as long as the tensile strength value is equal or above the minimum admissible value specified for the BM. Since this condition is not met, the welding parameters used in P1.0/S20 weld are not suitable to yield welds for structural applications.

Results of the tensile tests also allowed the calculation of the energy at break. Values of 112.8 J and 40.1 J for P2.0/S150 and P1.0/S20 welds were determined, corresponding to reductions of 26% and 74%, respectively, compared to 152.7 J for the BM. This rather small decrease in toughness in P2.0/S150 weld indicates that the chosen welding parameters (nominal power and travel speed) are suitable to produce welds for structural joint applications.

The strain hardening models summarized by Paruz and Edmonds (1989) were used to describe the uniform plastic behavior of P2.0/S150 and P1.0/S20 welds (Table 2).  $K$ ,  $n$ ,  $\sigma_0$ ,  $\epsilon_0$ ,  $A$  and  $B$  are material constants, while  $R^2$  is the adjusted R-squared curve fitting coefficient of determination. The highest values of  $R^2$  were those calculated by using the Voce model indicating a good description of the plastic behavior. The complex combination of dual-phase and weld microstructures makes difficult to model their plastic behavior by using Hollomon's model. Ludwik and Swift models displayed the lowest values of  $R^2$ . The mechanical behavior of P2.0/S150 weld was very similar to the one exhibited by the BM. It is worth mentioning that the strain-hardening parameters given by these models are larger in the welds than in the BM, in particular  $n$ . Nevertheless, these models can be useful to simulate TWB stamping using this steel.

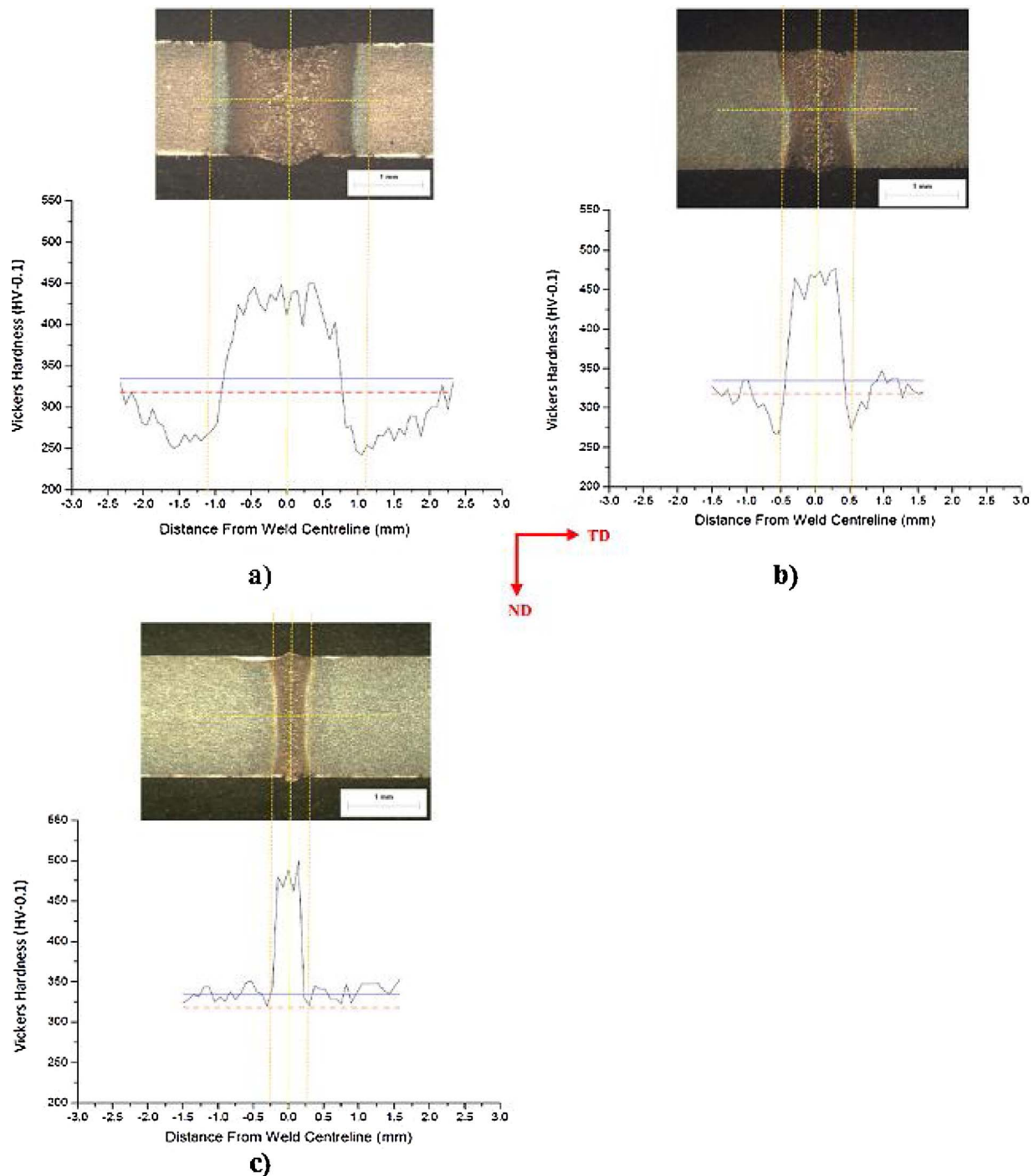


Fig. 7. Vickers hardness profile of the cross-section (TD-ND plane) of welds: a) P1.0/S20; b) P1.2/S50; and c) P2.0/S150. Light optical stereoscope image after etching with Nital 3%. TD e ND refer to the transverse and to the normal directions, respectively.

### 3.6. X-ray diffraction

P1.0/S20 and P2.0/S150 welds were examined by X-ray diffraction to quantify retained austenite (Table 3). Base metal does not contain retained austenite in the microstructure, while P1.0/S20 weld shows a volume fraction of retained austenite twice as high compared to sample P2.0/S150, showing that the broader the weld, the larger is the amount of retained

austenite. It is worth mentioning that these amounts of austenite are very close to the detection limit in XRD (about 3%). The presence of retained austenite was also confirmed by both LOM and EBSD.

### 3.7. Microstructural characterization

The microstructural characterization of P2.0/S150 weld was



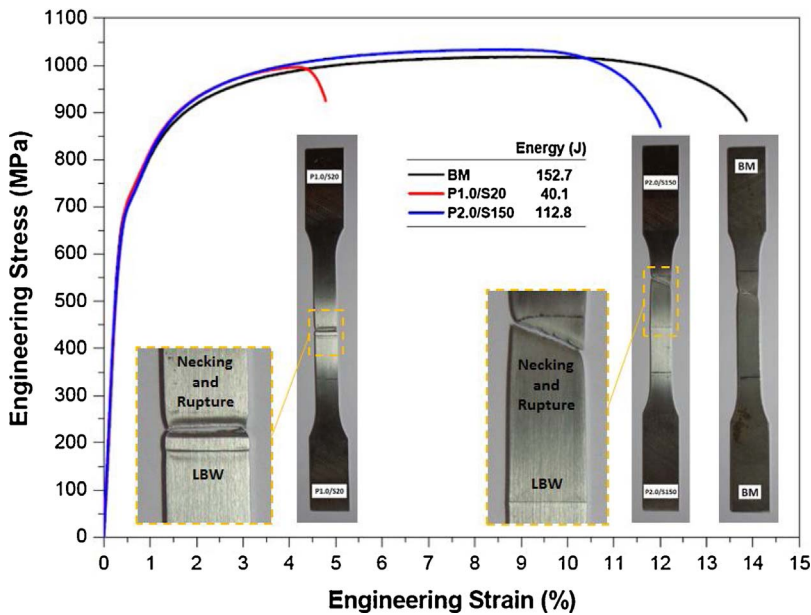


Fig. 8. Engineering stress-strain curves for the BM, P1.0/S20 and P2.0/S150 welds. The enlarged view of the necking regions is also depicted.

Table 2  
Fitting of experimental stress-strain data using different strain hardening models within the plastic regime from yield stress to tensile stress in BM and P2.0/S150 P1.0/S20 welds.

Model	Parameter	Result		
		BM	P2.0/S150	P1.0/S20
Hollomon $\sigma = K_H \varepsilon^{n_H}$	$K_H$	1624	1681	1888
	$n_H$	0.15	0.15	0.18
	$R_H^2$	0.971	0.967	0.981
Ludwik $\sigma = \sigma_0 + K_L \varepsilon^{n_L}$	$\sigma_0$	715	705	721
	$K_L$	1612	1687	4792
	$n_L$	0.54	0.52	0.81
	$R_L^2$	0.908	0.905	0.913
Swift $\sigma = K_S (\varepsilon + \varepsilon_0)^{n_S}$	$K_S$	1672	1733	2018
	$\varepsilon_0$	0.002	0.002	0.002
	$n_S$	0.15	0.16	0.20
	$R_S^2$	0.961	0.956	0.973
Voce $\sigma = B - (B - A) \cdot \exp(-n_V \varepsilon)$	$A$	1584	1629	1568
	$B$	1095	1109	1051
	$n_V$	53.8	56.7	83.8
	$R_V^2$	0.992	0.992	0.999

performed with different techniques and etchants. Fig. 9a shows the micrograph of the cross-section of the weld depicting the FZ after etching with modified LePera reactant. The clearest microconstituent is martensite whereas the brown microconstituent is probably bainite, taking into account the morphology and the likely high cooling rates experienced in this region. Fig. 9b, c shows the central region of the FZ after using different etchants, enabling to distinguish its microconstituents. The color contrast displayed in Fig. 9b reveals the presence of martensite and a second minor constituent. Contrary to the results reported by Saha et al. (2014) in DP980 welds, the microstructure of the FZ is not fully martensitic. Some martensite laths (dark brown) are lined up in the growth direction of columnar grains formed

Table 3  
XRD quantitative results of the volume fraction and lattice parameters of austenite and ferrite.

Sample	$\alpha$ -Fe		$\gamma$ -Fe	
	Volume fraction (%)	Cell parameter (nm)	Volume fraction (%)	Cell parameter (nm)
BM	100.0	0.2868	0.0	–
P1.0/S20	96.6	0.2866	3.4	0.3601
P2.0/S150	98.3	0.2866	1.7	0.3606

during solidification. The presence of an array of acicular structures which refers to either ferrite or bainite (light brown) is also noticed. Fig. 9c shows the presence of retained austenite (white phase) combined with martensite (blue) and either ferrite or bainite (brown). This microstructural arrangement is the so-called M-A constituent found in welded joints of several types of steels. Selective etching was also proposed by Alé et al. (1996) to identify M-A constituent in the HAZ of HSLA steels. A similar microstructural arrangement (M-A and bainite) was observed by Chen et al. (1984) using electrolytic etching to analyze the HAZ of a HSLA steel. Lambert et al. (2000) used mechanical polishing and chemical etching to image the microstructure of the HAZ in steel welds. Koyama et al. (2014) showed that the susceptibility to hydrogen embrittlement of DP steels can be attributed to ferrite and martensite microconstituents. Kasuya et al. (2013) highlighted that cold cracking occurs in martensite. They also poited out that retained austenite acts as an important trapping site for hydrogen in welds. Fig. 9d shows details of the grain refinement level promoted by martensitic transformation in the FZ. Despite the coarseness of the columnar grain structure formed upon solidification, the martensite laths found within grains are very thin, which explains the higher hardness of this constituent.

The transition region between intercritical and subcritical HAZs



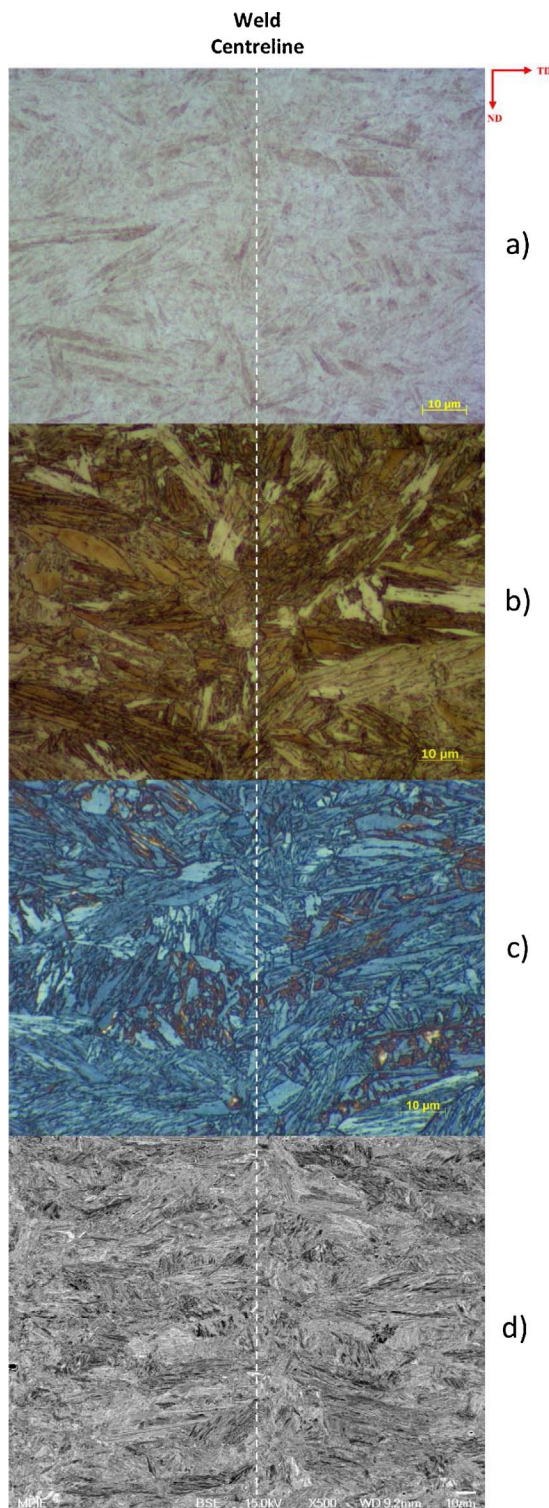


**Fig. 9.** Micrographs of the cross-section (TD-ND plane) of the P2.0/S150 weld in the FZ using different microscopy techniques and etchants: a) Light optical microscopy image after modified LePera etching; b) Light optical microscopy image after Nital 3% etching; c) Light optical microscopy image after etching with Klemm I reactant; and d) Scanning electron microscopy in the backscattered electrons image mode. TD e ND refer to the transverse and to the normal directions, respectively. (For interpretation of the references to color in the text, the reader is referred to the web version of this article.)

presented the so-called tempered martensite (TM) constituent, as shown in Fig. 10. The gradual variation in sharpness of color and contrast from the FZ towards the subcritical HAZ (SCHAZ) revealed the distinct response of ferrite and martensite to modified LePera etchant (Fig. 10a). Fig. 10b shows SEM micrograph of tempered martensite in the SCHAZ. It consists of partially-transformed martensite colonies displaying coarse carbides dispersed within the ferrite matrix.

### 3.8. Electron backscatter diffraction

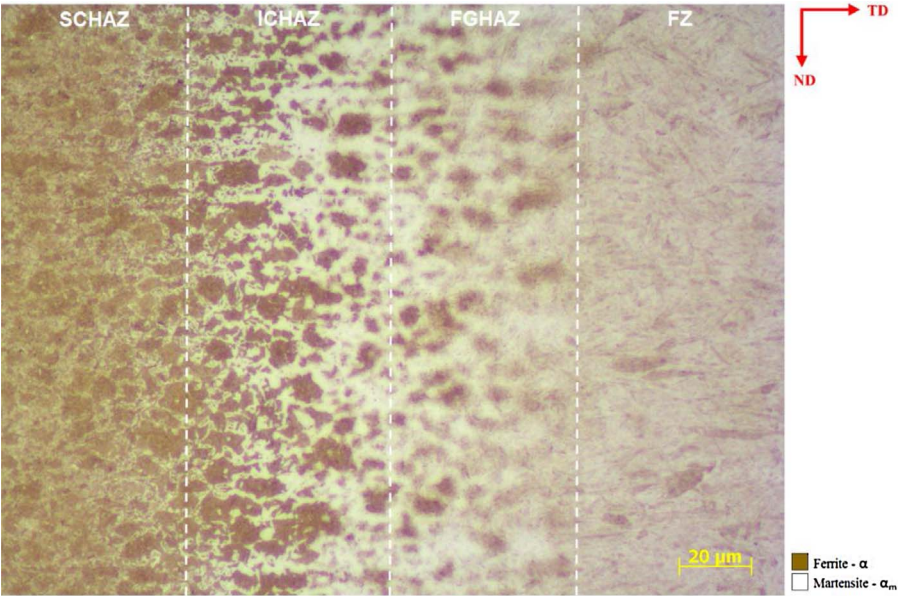
EBS mapping was conducted in P2.0/S150 weld. The analyzed area was  $160 \times 100 \mu\text{m}^2$  and comprises both the FZ and the HAZ. Fig. 11a shows the orientation imaging map highlighting the orientations of individual grains. The phase map presented in Fig. 11b shows how retained austenite is dispersed in the weld. Volume fraction and size of retained austenite increases from the FZ towards the HAZ. For quantitative analysis, four areas (A1, A2, A3 and A4) were selected along the welded joint, as shown in Fig. 11c. The image quality (IQ) map in Fig. 11c helps distinguishing each grain and the differences with regard to the microstructural refinement in the welded joint.

Fig. 12 shows an enlarged view of these four areas and their corresponding phase maps with regard to retained austenite. Areas A1, A2, A3 and A4 correspond to the FZ, fine-grained HAZ, intercritical HAZ and to the very end of the intercritical HAZ, respectively. Area A1 shows martensite and retained austenite with a volume fraction of 0.7%. This value must be considered in qualitative terms because some retained austenite at grain boundaries can be misindexed due to the overlap effects of Kikuchi patterns. Area A2 depicts the coexistence of fine and larger ferritic grains not fully transformed during welding because of the high welding speed and corresponding kinetic effects. The volume fraction of retained austenite is larger than in A1 (1.5%). In the area A3 the volume fraction of retained austenite is about 1.8%, accompanied by a noticeable increase in the size of the austenite islands, mostly found decorating the grain boundaries. A4 is the final portion of the intercritical HAZ where the material shows the highest softening after welding. The volume fraction of retained austenite is about 2.9% and it is found most at grain boundaries. Results are summarized in Table 4 where the phase volume fraction and the mean size of austenite islands determined by EBSD are shown.

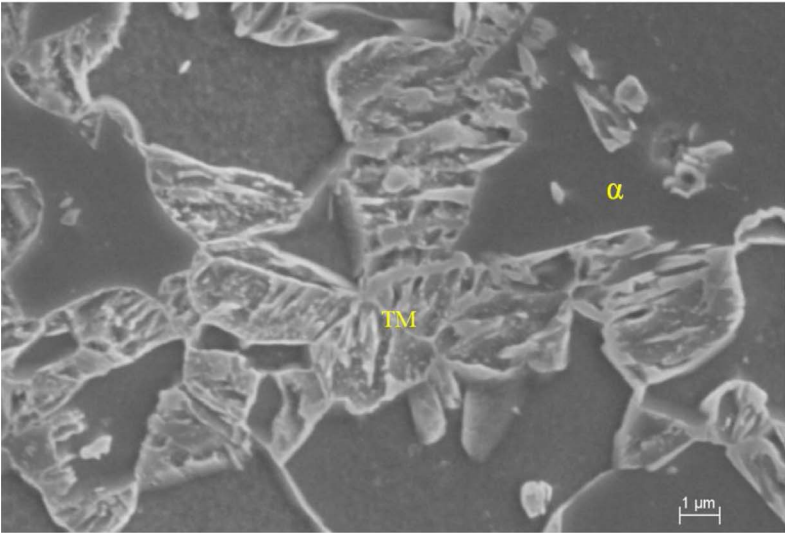
## 4. Conclusions

Laser beam welding was performed in DP1000 dual-phase steel sheets in a bead-on-plate configuration. The main conclusions are the following:

- The microstructure of the welds consists of martensite and ferrite (bainite) in the FZ. Retained austenite is found in all weld zones being more abundant in the transition zone between the intercritical and subcritical HAZs.
- Retained austenite and tempering of prior martensite are responsible for the softening experienced between intercritical and subcritical HAZs. Size and volume fraction of retained austenite increase from the FZ towards the HAZ.
- Sound welds with narrow HAZ can be produced using welding parameters that minimize both localized softening of prior martensite and volume fraction of retained austenite. P2.0/S150 weld fulfills these requirements being the soundest and most promising weld of all tested conditions.



a)



b)

**Fig. 10.** Micrograph of the cross-section (TD-ND plane) of the P2.0/S150 weld: a) Light optical microscopy image after modified LePera etching; and b) SEM micrograph after Nital 3% etching of the transition region between SCHAZ and ICHAZ (SE image mode). TD e ND refer to the transverse and to the normal directions, respectively. FZ – fusion zone, FGHAZ – fine grain HAZ, ICHAZ – Intercritical HAZ, and SCHAZ – subcritical HAZ.



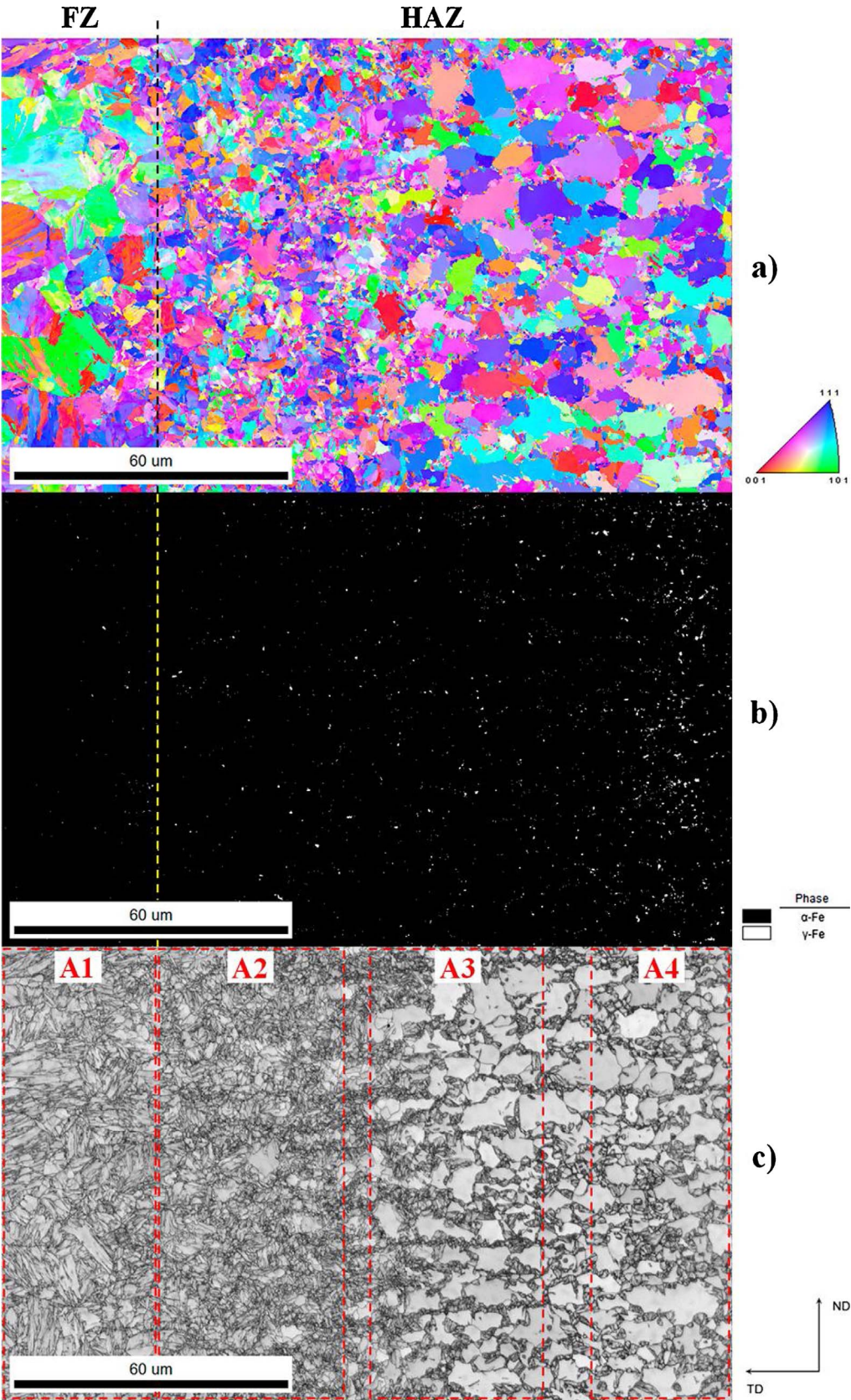


**Fig. 11.** EBSD maps of the welded joint P2.0/S150: a) Orientation image map; b) Phase map; and c) IQ map delineating the detailed regions A1, A2, A3 and A4.



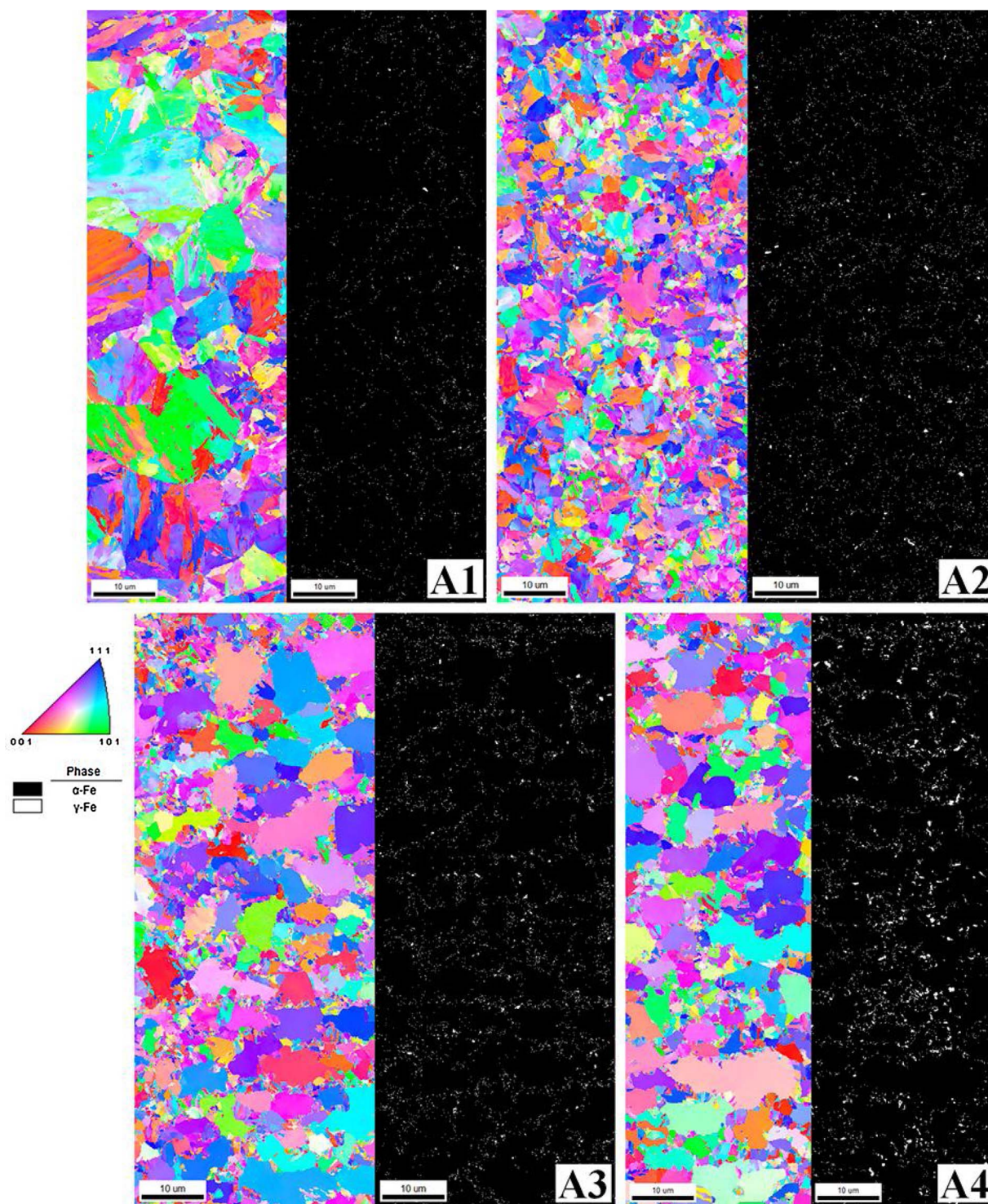


Fig. 12. EBSD maps corresponding to regions A1, A2, A3 and A4 of P2.0/S150 weld: a) Orientation image map; and b) Phase map. TD and ND refer to the transverse and to the normal directions, respectively.

### Acknowledgments

The authors are grateful to CNPq, Brazil (Grant 306.050/2013-7) for the partial financial support and to K. Angenendt and B. Breibach (MPIE, Germany) for their assistance in EBSD and capillary XRD

measurements, respectively. Thanks are also due to Prof. W. W. Bose Filho and Mr. D. Bon (EESC-USP, Brazil) for their assistance with the uniaxial tensile tests.



**Table 4**

Volume fraction and grain size of retained austenite of regions A1, A2, A3 and A4 of the welded joint P2.0/S150.

	Retained austenite			
	Mapped area			
	A1 (FZ)	A2 (FGHAZ)	A3 (ICHAZ)	A4 (ICHAZ/ SCHA2)
Fraction (%)	0.70	1.5	1.8	2.9
Grain size ( $\mu\text{m}$ )	$0.12 \pm 0.03$	$0.13 \pm 0.04$	$0.13 \pm 0.05$	$0.16 \pm 0.10$

## References

- ASM Committee, 1993. ASM Handbook Volume 1, Properties and Selection: Irons, Steels and High Performance. ASM International, Ohio, pp. 1394.
- AWS Committee, 2015. AWS D1.1/D1.1M: Structural Welding Code—Steel, Twenty-third ed. American Welding Society, pp. 112.
- Alé, R.M., Rebello, J.M.A., Charlier, J., 1996. A metallographic technique for detecting martensite-austenite constituents in the weld heat-affected zone of a micro-alloyed steel. *Mater. Charact.* 37, 89–93.
- Baltazar-Hernandez, V.H., Nayak, S.S., Zhou, Y., 2011. Tempering of martensite in dual-phase steels and its effects on softening behavior. *Metall. Mater. Trans. A Phys. Metall. Mater. Sci. Eng. A* 42, 3115–3129.
- Bandyopadhyay, K., Panda, S.K., Saha, P., Padmanabham, G., 2015. Limiting drawing ratio and deep drawing behavior of dual phase steel tailor welded blanks: FE simulation and experimental validation. *J. Mater. Process. Technol.* 217, 48–64.
- Bandyopadhyay, K., Panda, S.K., Saha, P., 2016a. Optimization of fiber laser welding of DP980 steels using RSM to improve weld properties for formability. *J. Mater. Eng. Perform.* 25, 1–16.
- Bandyopadhyay, K., Panda, S.K., Saha, P., Baltazar-Hernandez, V.H., Zhou, Y.N., 2016b. Microstructures and failure analyses of DP980 laser welded blanks in formability context. *Mater. Sci. Eng. A* 652, 250–263.
- Benyounis, K.Y., Olabi, A.G., Hashmi, M.S.J., 2005. Effect of laser welding parameters on the heat input and weld-bead profile. *J. Mater. Process. Technol.* 164–165, 978–985.
- Biro, E., McDermid, J.R., Embury, J.D., Zhou, Y., 2010. Softening kinetics in the sub-critical heat-affected zone of dual-phase steel welds. *Metall. Mater. Trans. A Phys. Metall. Mater. Sci. Eng. A* 41, 2348–2356.
- Bleck, W., Phiu-On, K., 2005. Microalloying of cold-formable multi phase steel grades. *Mater. Sci. Forum* 500–501, 97–114.
- Chen, J.H., Kikuta, Y., Araki, T., Yoneda, M., Matsuda, Y., 1984. Micro-fracture behaviour induced by M-A constituent (island martensite) in simulated welding heat affected zone of HT80 high strength low alloyed steel. *Acta Metall.* 32, 1779–1788.
- Easterling, K., 1992. Introduction to the Physical Metallurgy of Welding, Second ed. Butterworth-Heinemann, Oxford, pp. 133.
- Kasuya, T., Hashoba, Y., Inoue, H., Nakamura, S., Takai, K., 2013. Hydrogen diffusion in weld metals with retained austenite and its application to the welded joints. *Weld. World* 57, 581–593.
- Koyama, M., Tasan, C.C., Akiyama, E., Tsuzaki, K., Raabe, D., 2014. Hydrogen-assisted decohesion and localized plasticity in dual-phase steel. *Acta Mater.* 70, 174–187.
- Lambert, A., Drillet, J., Gourgues, A.F., Sturel, T., Pineau, A., 2000. Microstructure of martensite-austenite constituents in heat affected zones of high strength low alloy steel welds in relation to toughness properties. *Sci. Technol. Weld. Join.* 5, 168–173.
- Meng, W., Li, Z., Lu, F., Wu, Y., Chen, J., Katayama, S., 2014. Porosity formation mechanism and its prevention in laser lap welding for T-joints. *J. Mater. Process. Technol.* 214, 1658–1664.
- Parkes, D., Xu, W., Westerbaan, D., Nayak, S.S., Zhou, Y., Goodwin, F., Bhole, S., Chen, D.L., 2013. Microstructure and fatigue properties of fiber laser welded dissimilar joints between high strength low alloy and dual-phase steels. *Mater. Des.* 51, 665–675.
- Parkes, D., Westerbaan, D., Nayak, S.S., Zhou, Y., Goodwin, F., Bhole, S., Chen, D.L., 2014. Tensile properties of fiber laser welded joints of high strength low alloy and dual-phase steels at warm and low temperatures. *Mater. Des.* 56, 193–199.
- Paruz, H., Edmonds, D.V., 1989. The strain hardening behaviour of dual-phase steel. *Mater. Sci. Eng. A* 117, 67–74.
- Saeidi, N., Ashrafizadeh, F., Niroomand, B., 2014. Development of a new ultrafine grained dual phase steel and examination of the effect of grain size on tensile deformation behavior. *Mater. Sci. Eng. A* 599, 145–149.
- Saha, D.C., Westerbaan, D., Nayak, S.S., Biro, E., Gerlich, a. P., Zhou, Y., 2014. Microstructure-properties correlation in fiber laser welding of dual-phase and HSLA steels. *Mater. Sci. Eng. A* 607, 445–453.
- Wang, J., Yang, L., Sun, M., Liu, T., Li, H., 2016. Effect of energy input on the microstructure and properties of butt joints in DP1000 steel laser welding. *Mater. Des.* 90, 642–649.
- Xia, M., Biro, E., Tian, Z., Zhou, Y.N., 2008. Effects of heat input and martensite on HAZ softening in laser welding of dual phase steels. *ISIJ Int.* 48, 809–814.
- Xu, W., Westerbaan, D., Nayak, S.S., Chen, D.L., Goodwin, F., Biro, E., Zhou, Y., 2012. Microstructure and fatigue performance of single and multiple linear fiber laser welded DP980 dual-phase steel. *Mater. Sci. Eng. A* 553, 51–58.
- Yurioka, N., Suzuki, H., Ohshita, S., Saito, S., 1983. Determination of necessary pre-heating temperature in steel welding. *Weld. J.* 62, 147–153.
- Zhang, F., Ruimi, A., Wo, P.C., Field, D.P., 2016. Morphology and distribution of martensite in dual phase (DP980) steel and its relation to the multiscale mechanical behavior. *Mater. Sci. Eng. A* 659, 93–103.
- Zhao, Y.Y., Zhang, Y.S., Hu, W., 2013. Effect of welding speed on microstructure, hardness and tensile properties in laser welding of advanced high strength steel. *Sci. Technol. Weld. Join.* 18, 581–590.
- Zhou, J., Tsai, H.-L., 2007. Porosity formation and prevention in pulsed laser welding. *J. Heat Transf.* 129, 1014–1024.